

1 **Short summary.** 250 m estimates of snow water equivalent in the Western US and Canada are improved by assimilating
2 observations representative of a snow-focused satellite mission with a land surface model. Here, by including a gap-filling
3 strategy, snow estimates could be improved in forested regions where remote sensing is challenging. This approach improved
4 estimates of winter maximum snow water volume to within 4%, on average, with persistent improvements to both spring snow
5 and runoff in many regions.

6 **Extending the utility of space-borne snow water equivalent** 7 **observations over vegetated areas with data assimilation**

8 Justin M. Pflug^{1,2}, Melissa L. Wrzesien^{1,2}, Sujay V. Kumar², Eunsang Cho^{1,2,a}, Kristi R. Arsenault^{3,2}, Paul
9 R. Houser⁴, Carrie M. Vuyovich²

10 ¹Earth System Science Interdisciplinary Center, University of Maryland, College Park, MD, USA

11 ²Hydrological Sciences Laboratory, NASA Goddard Space Flight Center, Greenbelt, MD, USA

12 ³Science Applications International Corporation, McLean, VA, USA

13 ⁴Geography and Geoinformation Science Department, George Mason University, Fairfax, VA, USA ^acurrent address: Ingram
14 School of Engineering, Texas State University, San Marcos, TX, USA

15 *Correspondence to:* Justin Pflug (Justin.Pflug@nasa.gov)

16 **Abstract.** Snow is a vital component of the Earth system. Yet, no snow-focused satellite remote sensing platform currently
17 exists. In this study, we investigate how synthetic observations of snow water equivalent (SWE) representative of a synthetic
18 aperture radar remote sensing platform could improve spatiotemporal estimates of snowpack. We use a fraternal twin
19 Observing System Simulation Experiment, specifically investigating how much snow simulated using widely used models and
20 forcing data could be improved by assimilating synthetic observations of SWE. We focus this study across a 24°-by-37°
21 domain in the Western United States (US) and Canada, simulating snow at 250 m resolution and hourly timesteps in water-
22 year 2019. We perform two data assimilation experiments, including: 1) a simulation excluding synthetic observations in
23 forests where canopies obstruct remote sensing retrievals, and 2) a simulation inferring snow distribution in forested grid cells
24 using synthetic observations from nearby canopy-free grid cells. Results found that, relative to a nature run, or assumed true
25 simulation of snow evolution, assimilating synthetic SWE observations improved average SWE biases at maximum snowpack
26 timing in shrub, grass, crop, bare-ground, and wetland land cover types from 14%, to within 1%. However, forested grid cells
27 contained a disproportionate amount of SWE volume. In forests, SWE mean absolute errors at the time of maximum snow
28 volume were 111 mm, and average SWE biases were on the order of 150%. Here, the data assimilation approach that estimated
29 forest SWE using observations from the nearest canopy-free grid cells substantially improved these SWE biases (18%) and
30 the SWE mean absolute error (27 mm). Simulations employing data assimilation also improved estimates of the temporal
31 evolution of both SWE and runoff, even in spring snowmelt periods when melting snow and high snow liquid water content
32 prevented synthetic SWE retrievals. In fact, in the Upper Colorado River region, melt-season SWE biases were improved from

33 63% to within 1%, and the Nash Sutcliffe Efficiency of runoff improved from -2.59 to 0.22 . These results demonstrate the
34 value of data assimilation and a snow-focused globally relevant remote sensing platform for improving the characterization of
35 SWE and associated water availability.

36 **1 Introduction**

37 Snow plays important roles in the Earth system by regulating global temperatures and cooling the land surface because of
38 its reflective properties (Barry, 2002). Snow is also a major source of water storage for many regions, especially in areas that
39 rely on snowpack to sustain water resources during the dry season. In fact, it has been estimated that more than 2 billion people
40 around the world are reliant on seasonal snow melt for their water supply (Barnett et al., 2005). Snowpack is the natural
41 'integrator' of climatic conditions and offers more predictability of water availability than variables with shorter memory, such
42 as precipitation and streamflow (Terzago et al., 2023). Accurate wintertime estimates of snowpack are therefore critical for
43 water management and agricultural planning (Koster et al., 2010). For example, in the Western US, where a vast majority of
44 streamflow originates from snow (Li et al., 2017), it is common practice to use the April 1 snowpack, the historic date of
45 maximum snowpack in that region, for developing water supply estimates for later in the season. However, climate change
46 impacts have led to increased variability in the snow seasonality (Livneh and Badger, 2020), with warmer temperatures
47 reducing the amount of snow accumulation and seasonal snow storage, and advancing the timing of the spring melt. Therefore,
48 accurate characterization of winter snowpack and its variability is critically important for making informed water supply
49 quantifications.

50 In recognition of the critical need to have spatially distributed measurements of snow mass, there have been several efforts
51 to measure and estimate SWE from many different remote sensing platforms in the past several decades. Airborne lidar systems
52 have been able to provide high resolution, accurate measurements of snow mass (Painter et al., 2016), but this approach has
53 significant logistical barriers for global and frequent snow measurements, and the hydrological utility of a practical spaceborne
54 lidar platform is limited (Kwon et al., 2021). In the past three decades, snow depth and SWE estimates have been derived from
55 passive microwave remote sensing measurements, but these measurements are at coarse spatial resolutions, and have limited
56 accuracies over deep and wet snow, complex terrain, and dense vegetation (Derksen et al., 2014; Foster et al., 2005). Active
57 microwave remote sensing instruments such as Synthetic Aperture Radars (SARs) can provide finer spatial resolution
58 measurements to help resolve some of these issues. For example, C-band SAR observations from the Sentinel-1 constellation
59 have shown promise in obtaining high quality, moderate resolution (1km) observations in deep snow environments (Lievens
60 et al., 2019). A volume scattering radar approach, using X- and Ku-band SAR, has also been demonstrated in several airborne
61 campaigns and proposed for multiple snow mission concepts (Yueh et al 2009, Rott et al 2010) because of its potential to
62 achieve high resolution and global coverage over a range of snow depths. While these microwave instruments can observe in
63 night-time and cloudy conditions, they are still limited over areas with dense vegetation (Tsang et al., 2022). Further, all
64 spaceborne instruments have inherent coverage gaps due to their orbital and revisit configurations.

65 To overcome these limitations, modeling and data assimilation systems are needed that can extend the coverage and utility
66 of available measurements to areas, times, and variables that are not directly observed. In this article, we present a novel
67 approach through data assimilation, designed specifically to improve the usefulness of spaceborne SWE retrievals over forested
68 areas. The approach is demonstrated using an observing system simulation experiment (OSSE; e.g., Cho et al., 2023; Errico et
69 al., 2007) which is an approach used to formally assess the impact of the data to be collected from an anticipated mission.
70 Several prior studies have examined the use of OSSEs for snow mission studies (Garnaud et al., 2019; Kwon et al., 2021;
71 Wrzesien et al., 2022). Among them, SAR-focused OSSEs have been conducted by Garnaud et al. (2019) and Cho et al. (2023)
72 to assess the utility of hypothetical snow observations. Garnaud et al. (2019) focused on a Ku-band SAR to quantify trade-offs
73 between sensor configurations (e.g., various spatial resolutions and revisit frequencies) with retrieval algorithm accuracy and
74 SWE performance in southern Quebec, Canada, where temperate forests are dominant with shallow and moderate snowpack
75 conditions. Cho et al. (2023) conducted a X-/Ku-band SAR OSSE with an achievable sensor configuration (1 km spatial
76 resolution, 7-day revisit frequency, and orbital configurations) focusing on mountainous environments in a western Colorado
77 and testing the degree to which various SAR retrieval capabilities in different forest densities and snow volumes could improve
78 observationally-based SWE estimates. Here, we build on this prior research by developing an OSSE covering the entire
79 western US and portions of Canada. We simulate finer-scale (250 m) synthetic SWE observations that could be provided from
80 a future X-/Ku-band SAR mission, which are then incorporated within a land surface model through data assimilation to assess
81 their capability to improve snow state estimates, and the integrated impact on hydrologic states in space and time. The
82 assimilation experiments here are conducted with and without a novel strategy to extend SAR-based SWE estimates from
83 unforested regions into forested landscapes where SAR retrievals of the snowpack may be obscured by the forest canopy.

84 The primary contribution of this paper is the development of a viable strategy for extending hypothetical remotely sensed
85 SWE retrievals from a volume-scattering X-/Ku-band SAR satellite mission into difficult-to-observe forest landscapes. We
86 specifically focus on addressing the following research questions: 1) what is the added utility of spaceborne active remote
87 sensing SWE retrievals across the Western US and Canada? 2) how much can spatiotemporal representations of SWE be
88 improved by focusing on developing observationally based snow estimates over areas with dense vegetation, where SAR
89 sensors may be limited? 3) How much added hydrological utility can be obtained through spaceborne active remote sensing
90 measurements and data assimilation approaches, particularly when coverage over forested areas is improved?

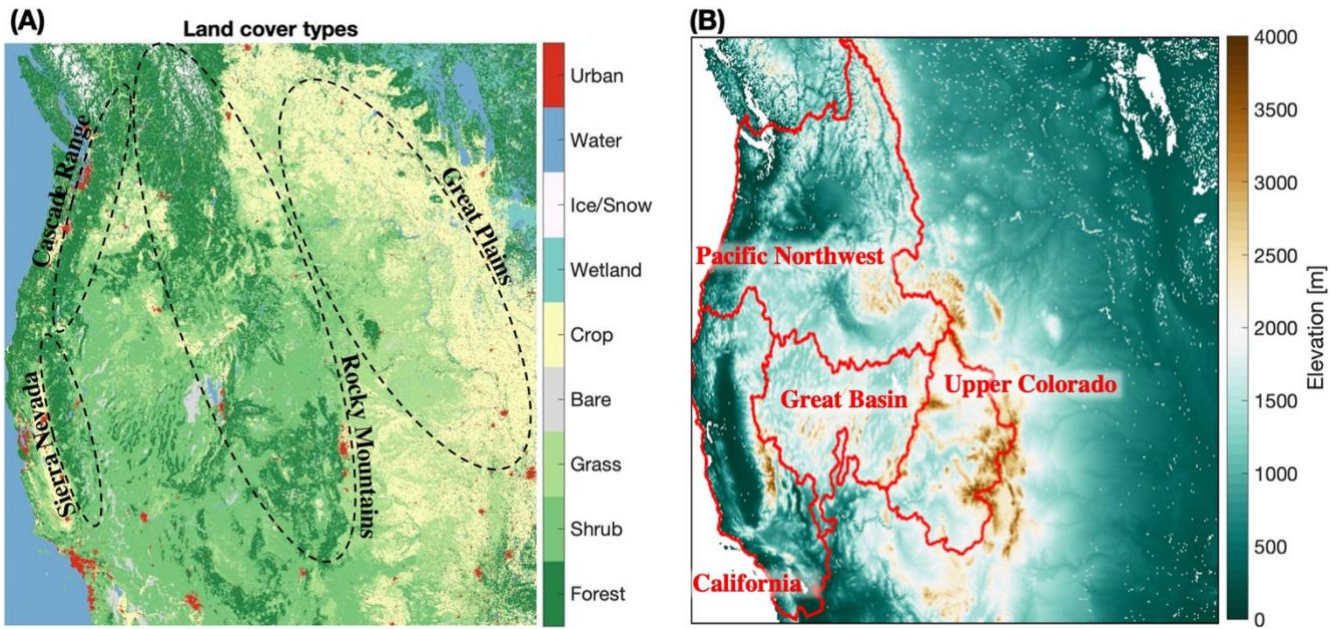
91 Section 2 describes the study domain and OSSE modeling setup. This is followed by the description of the results (Sect. 3),
92 a discussion of the findings (Sect. 4), and the study's conclusions (Sect. 5).

93 **2.1 Study domain and OSSE setup**

94 An OSSE is used to assess the value of the data to be collected from an anticipated mission. OSSEs often consist of the
95 following steps: 1) Developing a “nature run” that uses a state-of-the-art model employed with the best available boundary

96 conditions (Sect. 2.1); 2) using the nature run to generate simulated remote sensing observations, accounting for sources of
97 sensing limitations, sensing uncertainties, and orbital configurations (Sect. 2.2); 3) incorporating the simulated observations
98 (often through data assimilation, Sect. 2.3) in a separate, “open loop” model configuration with accuracies representative of
99 common modeling biases and uncertainties; and 4) evaluating how much the simulated remote sensing data improve the open
100 loop model performance relative to the nature run. In addition to this OSSE approach, this study goes further by 1) testing the
101 degree of improvement to both the remotely-sensed variable (i.e., SWE) and the resulting changes to land surface runoff in
102 snowy regions, and 2) developing two separate data assimilation experiments, one which masks simulated observations in
103 forested pixels where SAR retrievals may be most challenging, and the other including a novel approach for inferring SWE in
104 forested pixels using simulated observations from nearby, unforested pixels (Sect. 2.4). The details of the OSSE setup used in
105 this study are described in more depth throughout this section.

106 We employ the NASA Land Information System (LIS; Kumar et al., 2006), an infrastructure for high performance,
107 ensemble-based land surface modelling and data assimilation to enable this OSSE. LIS encompasses several advanced land
108 surface models that can simulate terrestrial water, energy, and carbon balances and related states such as soil moisture, land
109 surface temperature, and SWE, among others. These include different versions of community models such as Noah (Ek et al.,
110 2003), Variable Infiltration Capacity (VIC; Liang et al., 1994), Catchment (Koster et al., 2000), Joint UK Land Environment
111 Simulator (JULES; Best et al., 2011), and Noah-MP (Niu et al., 2011). The LIS framework also includes support for specialized
112 models that are designed to provide more detailed representations of certain land surface processes (e.g. snow), while enabling
113 interaction with LSMs that solve for water, energy, and carbon balances at a macroscale. For example, the advanced snow
114 physics model called SnowModel (Liston and Elder, 2006) has been incorporated within LIS in a manner that allows coupling
115 to existing LSMs. This structure allows the use of the advanced snow physics from SnowModel while leveraging the existing
116 process schemes (e.g., sub-surface, groundwater, canopy) within the LSMs. Here we utilize these unique capabilities for
117 enabling the OSSE integrations. . The study is conducted over a large domain (Fig. 1), covering the Western US and southern
118 Canada from 31-55N and 93-130W at a 250 m spatial resolution. As shown in Fig. 1, this modeling domain encompasses a
119 broad range of vegetation types, topographical regimes and water resources regions of the Pacific Northwest, California, Great
120 Basin, and Upper Colorado. 22% of the domain is covered by forests, with grasslands, croplands, and shrublands accounting
121 for 20%, 23%, and 26% of the domain, respectively. Forests dominate the coverage of areas with significant snowpack,
122 occupying 58% of regions that are in the mid-elevation range of 2500-3500m, and 15% of the areas with elevations over
123 3500m. From a modeling perspective, the domain extent of Fig. 1 (~83 million land grid points) is computationally challenging.
124 The scalable high performance computational and parallel inputting and outputting capabilities of NASA LIS were leveraged
125 to enable these simulations. A multiprocessor configuration involving approximately 1000 processors was employed to
126 facilitate large model simulations for the nature run, open loop simulation, and two simulations with data assimilation.



127
128
129
130

Figure 1: Maps of the land and vegetation classes (A; left panel) and elevation (in meters) (B; right panel) used in the simulations. Outlines and labels in the left panel indicate regions discussed in the Results (Sect. 4). Red contours in the right panel indicate hydrologic regions used in the analysis.

131
132
133
134

Simulations in this study are conducted by forcing LIS LSMs with the surface meteorology from NASA’s Modern Era Retrospective Reanalysis, version 2 (MERRA-2; Gelaro et al., 2017) and ECMWF Reanalysis, version 5 (ERA5; Hersbach et al., 2020) products. The model integrations were conducted for the water year 2019 (September 2018 – September 2019), which was a wetter than normal year based on the long-term average meteorological conditions over this domain.

135
136
137
138
139
140
141
142
143
144

The open loop and data assimilation integrations performed in this study are conducted using the Noah land surface model with multi-parameterization (Noah-MP) version 4.0.1 (Niu et al., 2011) and forcing from ERA5. The Noah-MP model evolved from the Noah LSM, with multiple options for various land surface processes. It represents energy, water, and carbon balances at the land surface by accounting for processes related to infiltration, evaporation, transpiration, runoff generation and groundwater recharge. A TOPMODEL-based runoff model (Beven et al., 2021) is used to calculate surface runoff and groundwater discharge. Options for prognostic vegetation dynamics models that represent the growth and senescence of vegetation are also available within Noah-MP. A two-stream radiative transfer approach is employed to calculate surface energy processes. Finally, a multilayer snowpack model (with up to three layers) is used to account for snow melt metamorphisms, compaction by overlying snow, sublimation of canopy intercepted snow, and snowmelt-refreeze cycles within Noah-MP (Niu and Yang, 2004).

145
146

Snow states like snow depth and SWE were also modeled across the Western US (domain highlighted in Fig. 1) at 250 m resolution and hourly time steps using a state-of-the-art and physically based single-layer snow model (named SnowModel;

147 Liston and Elder, 2006), provided forcing from MERRA-2 with LIS-provided lapse rates and topography-based meteorological
148 downscaling approaches, like incoming shortwave corrections based on topographical shading (Cosgrove et al., 2003; Kumar
149 et al., 2013). SnowModel has seen widespread use in the snow community, demonstrating the capability to resolve snow
150 evolution in a variety of landscapes and complex snow processes like the redistribution of snow via wind, and the resulting
151 impact on snow distribution, melt season snow duration, glacier mass balance, and snow habitat for species like polar bears
152 and Dall sheep (Hiemstra et al., 2002; Liston et al., 2016; Mahoney et al., 2018; Mernild et al., 2017; Sturm and Wagner,
153 2010). In addition to wind redistribution, snow evolution within SnowModel accounts for a wide set of snow processes,
154 including snow sublimation, snow grain size evolution, solar topographical shading, canopy shading, and canopy snow
155 interception. Through the coupling within LIS, Noah-MP snow states and the resulting snow-driven runoff were updated using
156 the SnowModel outputs at hourly timesteps for each grid cell.

157 Preliminary research has shown that relative to Noah-MP, LIS simulations coupling Noah-MP with SnowModel have
158 improved the volume and spatial distribution of simulated snow depth and SWE (Arsenault et al., 2021; Wrzesien et al., 2022).
159 Therefore, the coupled SnowModel and Noah-MP model was a prime candidate for the “nature run” in this study, or the
160 simulation most representative of the true underlying spatiotemporal snow states from which simulated observations were
161 derived (Sect. 2.2), and the assimilated model was compared against. Here, the nature run and open loop simulations detailed
162 above were compared to a widely-used Western US snow reanalysis product (Fang et al., 2022) to ensure that 1) the nature
163 run exhibited reasonable model accuracy, and 2) the departure between the open loop simulation and nature run are
164 representative of common regional, continental, and global modeling efforts (Figure S1 and S2). The OSSE developed for this
165 study is a “fraternal twin” OSSE, wherein two different models are used to simulate snow in the open loop (Noah-MP) and
166 nature run (SnowModel) simulations. This approach is selected since “identical twin” OSSEs, which use the same model, can
167 result in less divergence in model states and information content, biasing the degree of model improvement that could come
168 from assimilating an observation (e.g., Yu et al., 2019). More information on the difference between the open loop and nature
169 run models can be found in Table S1.

170 **2.2 Observation simulator**

171 Synthetic SWE retrievals at 250 m spatial resolution, representative of a hypothetical X- and Ku-band SAR mission, are
172 simulated from the nature run. To do this, the orbital swaths are simulated using TAT-C (Le Moigne et al., 2017). TAT-C is a
173 NASA software system designed for future Distribution Spacecraft Missions (DSM), which enables us to explore a range of
174 feasible design options (e.g., constellation vs. single, geostationary vs. polar-orbiting, low vs. high temporal frequencies) to
175 estimate optimal gains for the given mission configuration. Previous OSSEs have been conducted to test the impact from
176 different snow mission configurations (e.g. Garnaud et al 2019). Here we instead focus on demonstrating the value of a gap-
177 filling approach (Sect. 2.4) for estimating snow in forested landscapes where SAR retrievals may be most challenging.
178 Therefore, we used TAT-C to design a conservative mission configuration consisting of a small constellation of X- and Ku-

179 band SAR satellites. Using a 10-14 day revisit frequency, depending on latitude, TAT-C orbital swaths were applied to the
180 nature run outputs to simulate the satellite viewing area. The remote sensing spatial coverage is simulated by extending the
181 ground track to a swath width. The daily viewing extents are then simulated as a daily binary map (so-called “cookie cutter”)
182 masking the surface as viewed or not at a 250 m spatial resolution.

183 Based on an error level of 20%, spatially and temporally uncorrelated random errors drawn from a Gaussian distribution are
184 added to the synthetic SWE retrievals. This 20% error level is selected using a conservative estimate of SWE measurement
185 uncertainty for a volume-scattering X-/Ku -band SAR mission based on developed mission design concepts and ground
186 validation. For example, the ESA Cold Regions Hydrology High-Resolution Observatory (CoREH2O) mission expected to
187 meet instrument and retrieval requirements of ± 30 mm accuracies for SWE of 300 mm, $\pm 10\%$ for SWE greater than 300 mm
188 (Rott et al 2010, 2012). Similarly, the Canadian Terrestrial Snow Mass Mission (TSMM) concept that is currently under
189 development aims to achieve better than 20% measurement uncertainty for SWE greater than 50 mm, though it is limited to
190 SWE less than 200 mm due to the dual Ku-band system (Garnaud et al. 2019). Airborne and tower-based field data have
191 demonstrated that a combination X- and Ku-band system can provide SWE retrievals over a range of snow conditions at
192 accuracies better than 20% (Zhu et al. 2018, 2021, Tsang et al 2022, Durand et al. 2023, Singh et al. 2023). However, we use
193 an assumption of uniform error levels throughout the domain, whereas in reality, the errors are likely to be dependent on other
194 factors, including the terrain characteristics, snow characteristics, and vegetation. This is discussed more in Section 4.

195 **2.3 Data assimilation setup**

196 A one-dimensional ensemble Kalman Filter (EnKF; Reichle et al., 2002) is used to assimilate the synthetic observations
197 within the open loop configuration of the model. EnKF is widely used for land data assimilation studies (Kumar et al., 2022),
198 as it provides a flexible approach for the treatment of model and observation errors and non-linear models. An ensemble of
199 model realizations is used by EnKF to assess and propagate model errors. In this instance, the ensemble requirement further
200 adds to the significant computational requirements of the large model domain (Fig. 1) and fine spatial resolution of the
201 simulations (250 m). Therefore, a 5-member ensemble with perturbations applied to the meteorological variables and model
202 prognostic fields are used for simulating uncertainty in the modeled estimates. Table 1 details the parameters for meteorological
203 and model state perturbations, which are based on recent snow data assimilation studies (Lahmers et al., 2022; Kwon et al.,
204 2021). Though a larger ensemble size is better for ensuring sufficient sampling density, our choice of five ensembles is
205 reasonable given that the model state vector used in the assimilation only consists of two variables; the total SWE and snow
206 depth. The assimilation setup employs a sequential update strategy, where at each time step an ensemble of model forecasts is
207 propagated forward in time, followed by an update based on observational inputs. The model states are updated toward the
208 observations based on the relative uncertainties in the model and observations using the following formulation, at a certain
209 time k .

210

$$x_k^{i+} = x_k^{i-} + K_k [y_k^i - H_k x_k^{i-}] \quad \text{Eq. (1)}$$

211

212

213

214

Where x_k and y_k are the model and observation state vectors, respectively. The term H_k represents the observation operator that maps the model states to the observed variables. The superscripts $i -$ and $i +$ represent the i th ensemble member before and after the update, respectively. K_k is the “Kalman gain” term, that allows the weighting of the observations and model forecasts is a function of the model and observation error covariances.

215

Table 1. Model forcing and state-variable perturbations used by the 5-member ensemble of LIS simulations

Variable	Perturbation Type	Std. Dev.	Cross Correlation across variables			
			SW corr	LW corr	PCP corr	T corr
Meteorological Forcing						
Downward Shortwave (SW)	Multiplicative	0.2	1	-0.3	-0.5	0.3
Downward Longwave (LW)	Additive	30	-0.3	1	0.5	0.6
Precipitation (PCP)	Multiplicative	0.5	-0.5	0.5	1	-0.1
Near surface Air Temperature (T)	Additive	0.5	0.3	0.6	-0.1	1
Noah-MP LSM snow states			SWE	Snow depth		
SWE	Multiplicative	0.01	1	0.9		
Snow depth	Multiplicative	0.01	0.9	1		

216

217

218

219

220

221

222

223

224

The data assimilation procedure detailed here assimilated the synthetic SWE retrievals (Sect. 2.2) with the open loop simulation. The degree to which the simulation with data assimilation approached SWE simulated by the nature run is intended to represent the extent to which a SAR remote sensing platform with the SWE retrieval characteristics from Sect. 2.2 could be combined with a land surface model to provide near real-time estimates of SWE at 250 m resolution. However, the SAR observations synthesized in this study have known issues with observing snow with high liquid water contents and dense forest cover. Therefore, synthetic observations at each timestep were masked at grid cells where the most-dominant landcover type from the North American Land Change Monitoring System (NALCMS; Latifovic et al., 2017) was forested, including deciduous, evergreen, and mixed forest cover (Fig. 1). Synthetic observations were also masked at grid cells where and when

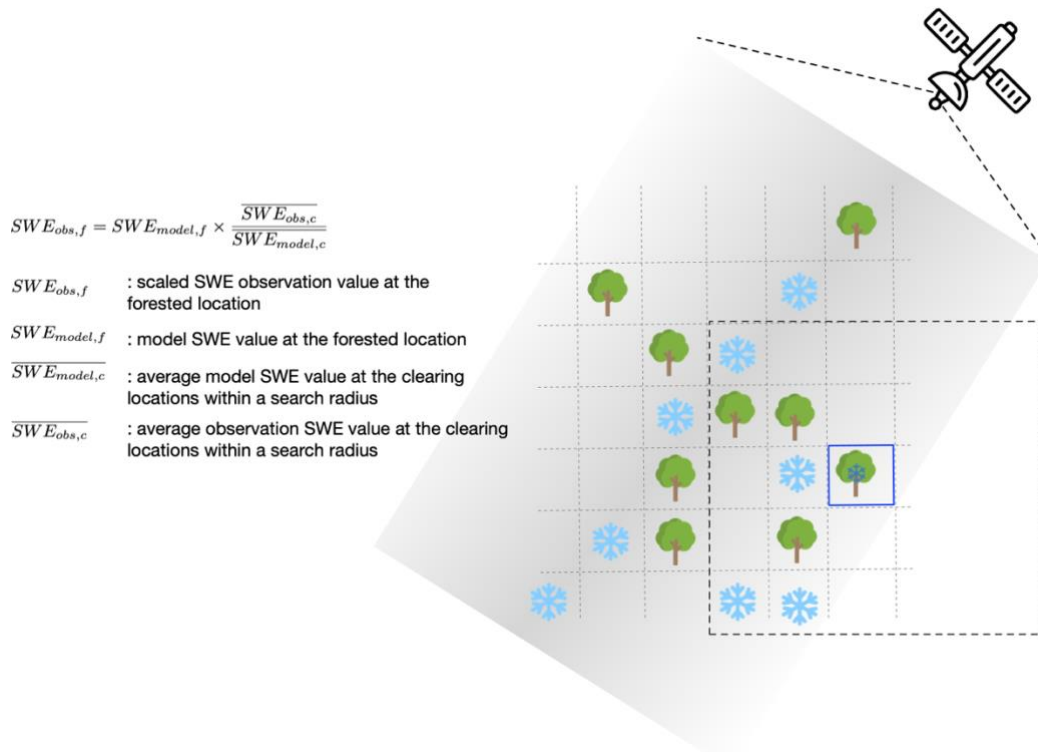
225 snow was experiencing melt, identified by the presence of liquid water in the snowpack from the nature run. Although limited
226 in area, grid cells with “ice” landcover (Fig. 1) were also excluded. In this study, this simulation which used assimilation only
227 in unforested, non-melting, and ice-free grid cells is termed “Data Assimilation, without the forest strategy” (DA). In Sect. 2.4
228 below, we present a novel approach used to infer SWE in grid cells with forests using the nearest canopy-free synthetic
229 observations.

230 **2.4 Extending observations over forests**

231 The 1-d EnKF approach employed here updated each model grid SWE from the open loop simulation based on the
232 observations available at that grid point. Though studies have employed 3-d EnKF approaches to spatially propagate
233 observational information to neighbouring grid cells (De Lannoy et al., 2012), here we relied on 1-d updates due to several
234 factors. First, a 2-d update requires the knowledge of spatial error correlations and their variability, which is challenging to
235 specify (Ying, 2020). Most prior studies using such schemes employ uniform specifications and are limited to small domains.
236 Second, a 2-d update increases the size of the state vector and consequently requires the use of a larger ensemble. This,
237 combined with the added computational expense of a 2-d analysis significantly increases the computational cost. Therefore,
238 we employed an alternate approach that is computationally more efficient while allowing the extension of observations to
239 nearby areas.

240 Assuming that the SWE retrievals from the hypothetical SAR instrument are limited over areas where the dominant
241 vegetation type are forests (Fig. 1a), we employ a novel approach to extend the observations obtained in non-forested areas
242 (Fig 2). For every forested location, valid retrievals over nearby non-forested locations within a radius of influence of 750 m
243 are identified. An observation at the forested pixel is then estimated by scaling the model SWE by the ratio of the average
244 observed SWE to modeled SWE over the ‘clearing’ areas (Fig. 2). This scaled observation is then used for assimilation over
245 the forested pixel. Here we implicitly use the spatial correlations inherent in the model between forested and clearing areas to
246 extend observational coverage over the clearing to forested locations. This simulation is termed “Data Assimilation, with the
247 forest strategy” (symbolized by DA+F in Section 3). To evaluate the accuracy and added value of this scaling approach, we
248 compare SWE and runoff from the nature run simulation, versus simulations with data assimilation both 1) employing the
249 forest scaling strategy discussed here, and 2) masking synthetic observations in forested grid cells (Sect. 2.3).

250



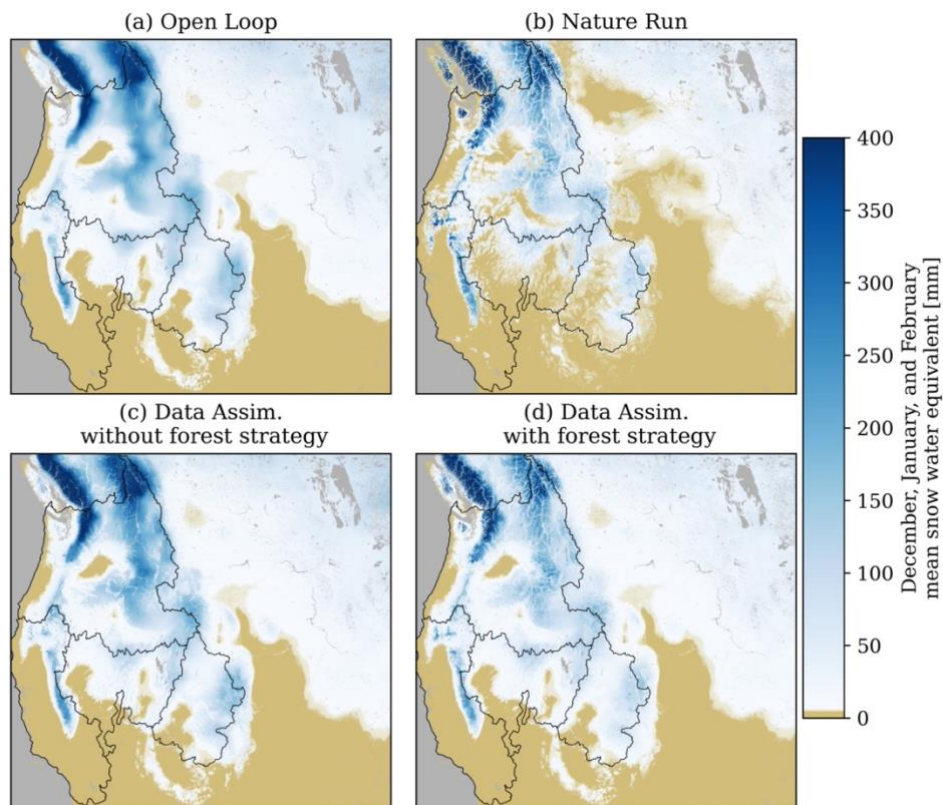
251

252 **Figure 2.** Conceptual depiction and equations demonstrating the forest strategy used here, which estimates a SWE observation
 253 at a given grid cell (outlined box in blue color) based on the modeled SWE ($SWE_{model,f}$) and the ratio between the average
 254 synthetic SWE observations ($\overline{SWE_{obs,c}}$) and average modeled SWE ($\overline{SWE_{model,c}}$) from grid cells within a 750 m radius
 255 (dashed box). The light gray shading represents the satellite swath, the tree icons indicate forested locations, and the snowflake
 256 icons represent grid cells with valid SWE retrievals at non-forested locations. The grid cell from this example is near the
 257 satellite swath edge, so observations are unavailable in the nearby regions South and East of this pixel.

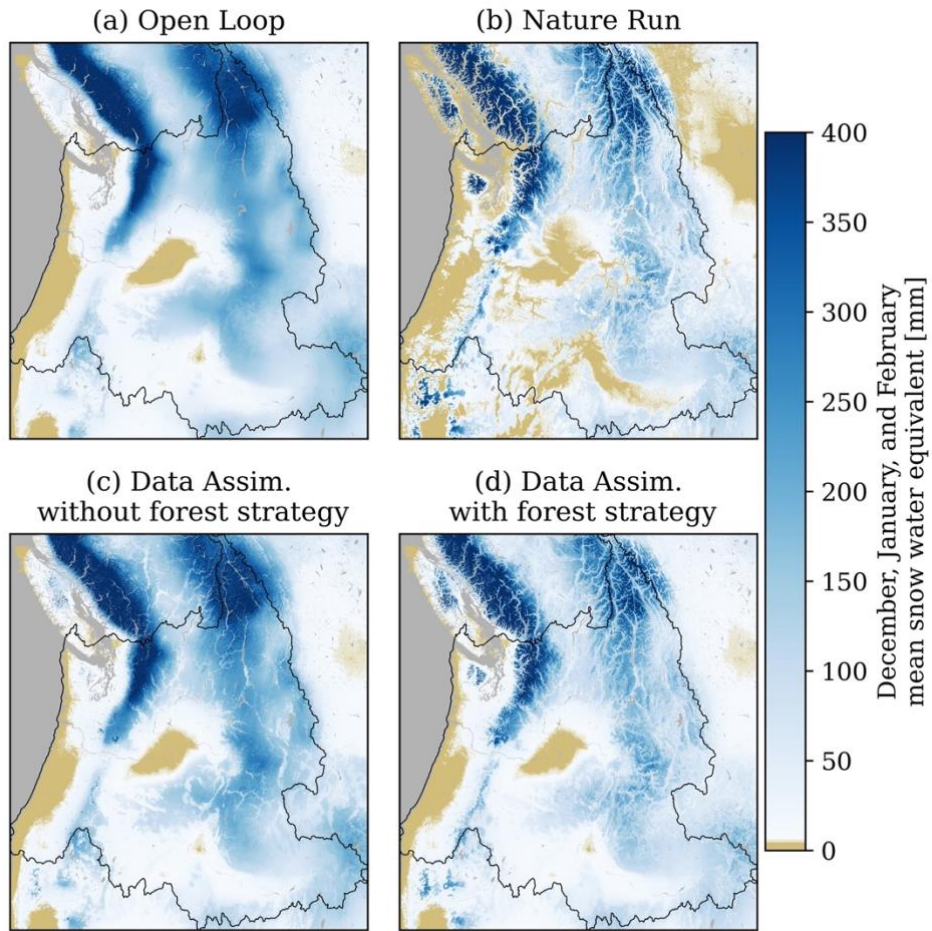
258 3 Results

259 In this section, we compute the difference between the open loop simulation, nature run, and the two open loop simulations
 260 with data assimilation, one masking synthetic observations over regions with forests, and time periods with melting snow, and
 261 ice, and the other applying the same data assimilation but extending snow estimates in forested regions using the strategy from
 262 Sect. 2.4 and Fig. 2. The differences between these simulations are detailed in Section 2 and Table S1. We focus on the
 263 differences between these four simulations using: 1) average SWE from the winter snow accumulation season (December,
 264 January, and February; DJF), when snowmelt is minimized and synthetic observations are masked by grid cells with liquid
 265 water content to the smallest degree, 2) spatially distributed SWE on 13 March, the date corresponding to the timing of
 266 maximum SWE volume in water-year 2019, and 3) daily average SWE and total runoff for each day in water-year 2019 over
 267 a number of selected hydrologic regions including the Pacific Northwest, California, Great Basin, and Upper Colorado (Fig.
 268 1b).

269 The open loop and nature run simulations exhibited differences in both the volume and spatial distribution of average winter
270 (December, January, and February; DJF) SWE (Fig. 3a and 3b). Relative to the nature run, the open loop simulation tended to
271 simulate lower elevation winter SWE that was both larger in magnitude and persisted for longer before melting. In the Pacific
272 Northwest domain (Fig. 4), DJF average snow cover (defined as grid cells with mean DJF SWE exceeding 5 mm), was
273 approximately 12% larger for the open loop simulation than the nature run (Table 2). These snow extent biases were also
274 apparent in the other hydrologic regions (Figs. S3 – S5), where open loop snow extents exceeded snow extents from the nature
275 run by 26% in the Upper Colorado, 45% in the Great Basin, and 6% in California. Visually, the nature run had significant
276 increases in the spatial variability of winter SWE, better representing the differences in SWE between mountain peaks and
277 valleys, and the patchiness of snow cover in regions with winter snowmelt and ephemeral snow cover (e.g., Fig. 4, Fig. S1).
278 Relative to the nature run, DJF SWE from the open loop simulation was biased high across the full modeling region (Fig. 3)
279 by approximately 26%, on average, with a mean absolute error of 41 mm and spatial coefficient of correlation of approximately
280 0.74. Across the Pacific Northwest (Fig. 4), DJF mean SWE biases were approximately 37%, with a mean absolute error of
281 55 mm. Open loop model performance for the other hydrologic regions can be found in Table 2.



282
283 **Figure 3.** Winter (December, January, and February) mean SWE simulated at 250 m resolution from the open loop (a), nature
284 run (b), and data assimilation simulations, both with (d) and without (c) the forest strategy presented in Sect. 2.4.



285

286

287

288

Figure 4. Winter (December, January, and February) mean SWE in the Pacific Northwest region simulated at 250 m resolution from the open loop (a), nature run (b), and data assimilation simulations, both with (d) and without (c) the forest strategy.

289
290
291

Table 2. Simulation performance, relative to the nature run simulation, for the open loop simulation (OL) and the simulations with data assimilation, both with (DA+F) and without (DA) the forest strategy. Statistics are presented for the full domain, the four hydrologic regions, and all forested and unforested grid cells.

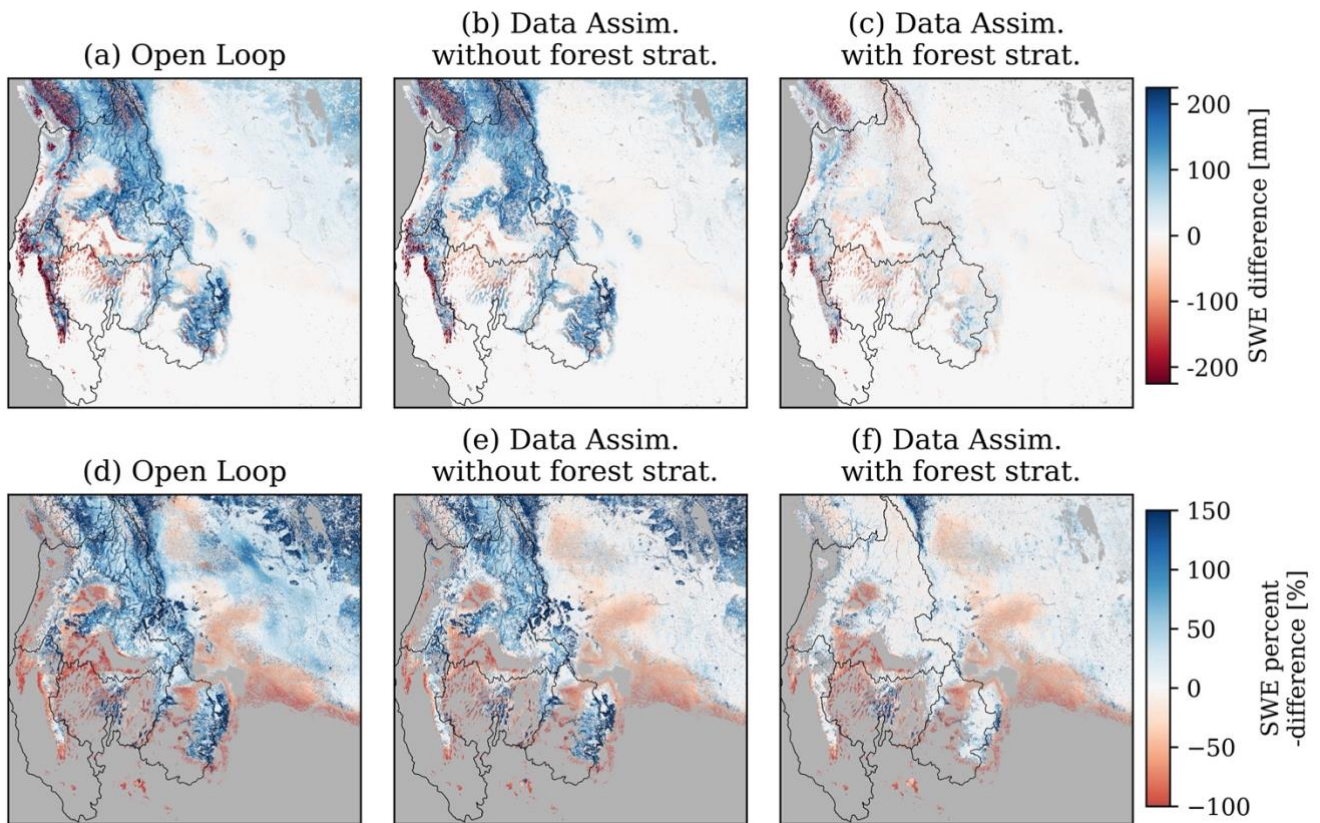
		DJF* snow- extent biases	13 March 2019 SWE			Seasonal SWE and runoff	
			Mean bias	SWE abs. error [mm]	Coeff. of corr.	MAM* mean SWE bias	Nash- Sutcliffe Efficiency
Full study domain	OL [^]	+22%	+26%	41	0.74	-	-
	DA [^]	+23%	+9%	36	0.79	-	-
	DA+F [^]	+22%	+4%	17	0.91	-	-
Upper Colorado	OL	+26%	+37%	55	0.74	+63%	-2.59
	DA	+28%	+27%	50	0.74	+86%	-3.71
	DA+F	+28%	+8%	23	0.90	< 1%	0.22
Pacific Northwest	OL	+12%	+42%	89	0.69	+44%	-0.17
	DA	+13%	+32%	80	0.74	+80%	-0.34
	DA+F	+13%	+6%	35	0.89	+15%	0.39
Great Basin	OL	+45%	+35%	38	0.62	-29%	0.58
	DA	+46%	+46%	32	0.75	+10%	0.58
	DA+F	+46%	+28%	23	0.83	-38%	0.53
California	OL	+6%	-34%	50	0.64	-50%	0.92
	DA	+8%	-6%	40	0.79	-15%	0.88
	DA+F	+8%	-6%	28	0.88	-26%	0.89
Unforested	OL	+19%	+14%	22	0.83	-	-
	DA	+20%	< 1%	14	0.91	-	-
	DA+F	+20%	< 1%	14	0.91	-	-
Forested	OL	+29%	+150%	111	0.67	-	-
	DA	+30%	+150%	111	0.67	-	-
	DA+F	+30%	+18%	27	0.93	-	-

* DJF = December, January, and February; MAM = March, April, and May (averages)
[^] OL = open loop simulation; DA = data assimilation without the forest strategy; DA+F = data assimilation with the forest strategy

292 As expected, the simulations assimilating the synthetic SWE observations agreed with the nature run better than the open
 293 loop simulation. However, on 13 March 2019 (the date of maximum domain SWE volume), the simulation with data
 294 assimilation without the forest strategy had high-biased SWE across large portions of the Rocky Mountains and the Cascade
 295 Mountain range (Fig. 1, Fig. 5b and Fig. 5e). Low biased SWE was more common in Northernmost Canadian portions of the
 296 Rocky Mountains and Cascade Range, the Western montane regions in Washington State, the Northern portions of the Great
 297 Basin, and the lower-lying elevations of the California Sierra Nevada. Additionally, despite the assimilation, snow extents
 298 were still biased high relative to the nature run (Fig. 3) at magnitudes similar to the open loop simulation (Table 2). This was
 299 driven by the expansive snow extents of the open loop simulation, which were decreased by data assimilation, but still resulted
 300 in widespread early-season SWE increases for short periods of time between synthetic observations (at 10 – 14 day

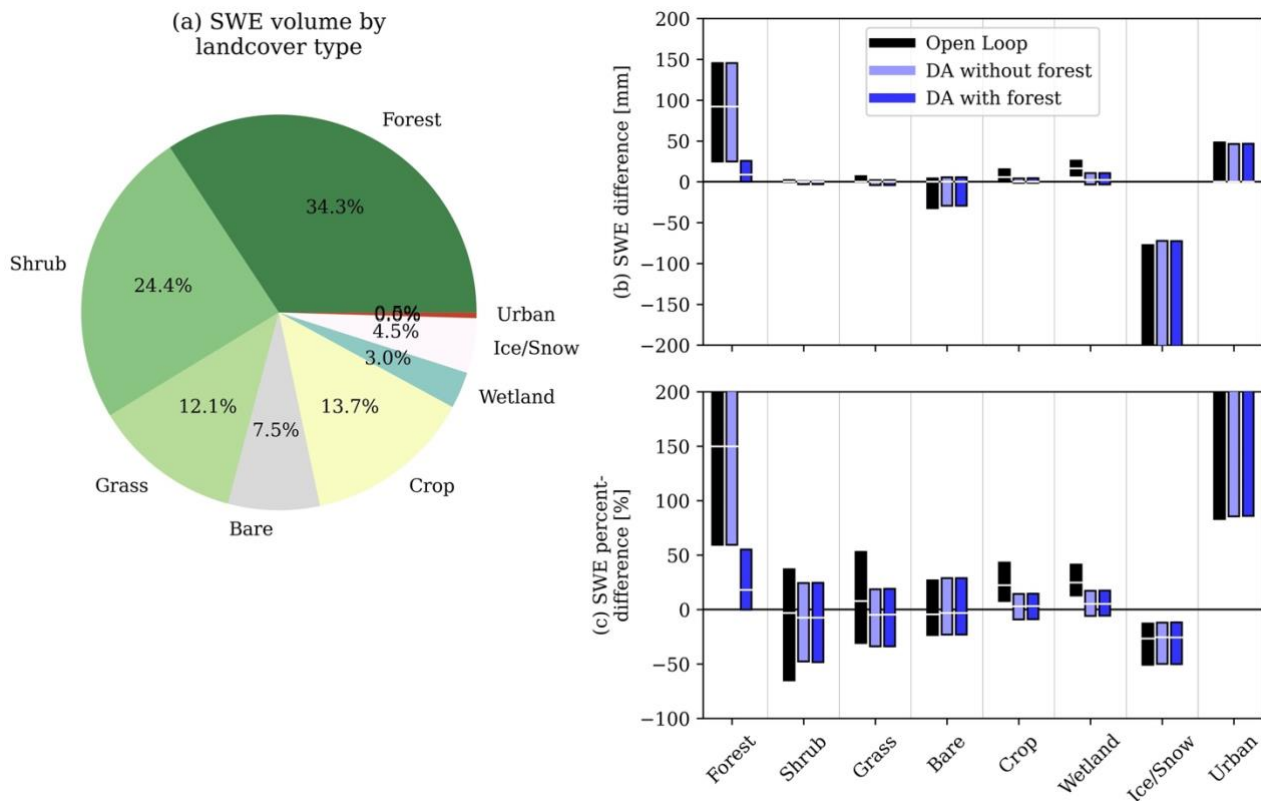
301 frequencies), increasing to the number of grid cells with DJF SWE exceeding 5 mm (threshold used to define average winter
302 snow extents in Fig. 3).

303 Assimilating the synthetic SAR observations without the forest strategy best improved SWE in shrub, grass, crop, bare, and
304 wetland landcover types (Fig. 6b and 6c). For example, relative to the open loop simulation (Fig. 5a and 5d), data assimilation
305 without the forest strategy (Fig. 5b and 5e) corrected the high SWE biases in the Great Plains (Fig. 1). While 13 March SWE
306 in shrub, grass, crop, bare-ground, and wetland regions was typically small in magnitude, these landcover types accounted for
307 77% of the modeling domain area, and 61% of the domain total SWE volume on 13 March (Fig. 6a). In these regions, SWE
308 from the open loop simulation had a mean absolute error of 22 mm, and a mean bias of approximately 14%, relative to the
309 nature run (Table 2). Data assimilation significantly improved the SWE bias in these land cover types to within 1%, on average
310 (Fig. 6b), with a mean absolute error of 14 mm, relative to the nature run.



311
312 **Figure 5.** 13 March 2019 SWE difference (top row) and percent-difference (bottom row), relative to the nature run, for the
313 open loop simulation (a and d), and simulations with data assimilation, both with (c and f) and without (b and e) the forest
314 strategy. SWE percent-difference maps (bottom row) only compare grid cells where SWE from the nature run was greater
315 than 5 mm.

316 The data assimilation results discussed above did not use the synthetic observations over forested grid cells, where
317 retrievals from SAR instruments may be either partially or fully occluded by the canopy overstory (Tsang et al., 2022; Ruiz
318 et al., 2022; Huang et al., 2019). However, a significant portion of the snow volume in mid-latitude domains overlaps with
319 forests. For example, although forests only covered approximately 22% of the study region investigated here (Fig. 1a),
320 forested grid cells contained just over 34% of the total 13 March SWE volume, a volume about 10% higher than the snow
321 volume contained in the next-largest landcover type (Fig. 6a). In forested grid cells, SWE simulated by the open loop
322 simulation were biased high by approximately 87 mm (+150%) on average (Fig. 6), with a mean absolute error of 111 mm
323 (Table 2). These errors were propagated into the simulation with data assimilation without the forest strategy. Fortunately,
324 the ratio between modeled SWE and synthetic SWE observations in forested grid cells and the nearest canopy-free grid cells
325 had high levels of similarity. Therefore, estimating snow in forest regions using the nearest canopy-free pixels (Fig. 2)
326 improved snow simulations significantly (Fig. 3d, Fig. 4d, and Fig. 5c and 5f). In fact, snow simulated in forest landscapes
327 using data assimilation with the forest strategy agreed well with the nature run, exhibiting a 13 March SWE average bias in
328 forested grid cells of only 14 mm (+8%) (Fig. 6), and a mean absolute error of 27 mm. This forest strategy resulted in large-
329 scale improvements to total domain SWE (Fig. 5), reducing the 13 March full-domain SWE volume bias by 28%, and
330 improving the spatial coefficient of correlation by 0.12, relative to the data assimilation simulation without the forest
331 strategy.

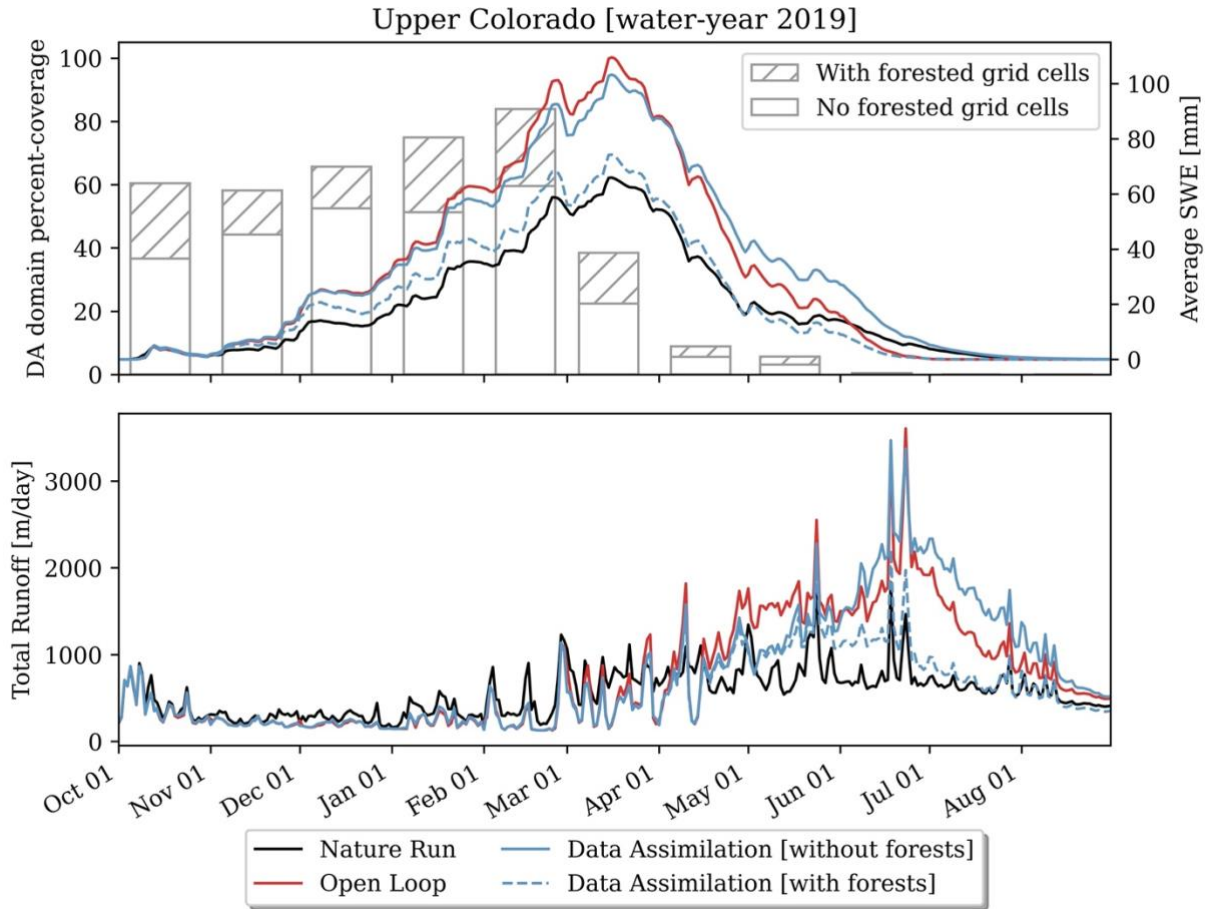


332

333 **Figure 6.** SWE volume on 13 March 2019 broken down by landcover type in subplot a. For each landcover type, the
 334 interquartile range and median of SWE differences (b) and SWE percent-differences (c) are calculated for the open loop
 335 simulation (black) and each simulation with data assimilation (blue bars). SWE differences (b) and (c) are calculated relative
 336 to the nature run.

337 The comparisons above focused on mean DJF SWE and SWE from the date nearest maximum snow volume (13 March,
 338 2019). However, assimilating the synthetic SWE data also improved estimates of snow water resources throughout the
 339 duration of the water year, even in periods when most snow-covered regions were experiencing snowmelt and synthetic
 340 observations were masked. For example, in the Upper Colorado, approximately 75% of the region had DJF snow cover with
 341 little or no winter snowmelt (Fig. 7). The simulation with data assimilation and the forest strategy substantially improved
 342 mean SWE evolution in the snow accumulation season in this hydrologic region (Fig. 7, October - March). However,
 343 snowmelt onset in the March, April, and May (MAM) months increased the number of grid cells experiencing snowmelt
 344 from the open loop model outputs, reducing the number of grid cells across the full Upper Colorado Region that could be
 345 observed by the synthetic SAR observations to approximately 5%, on average, over this period of time. Despite this, since
 346 the simulation with data assimilation improved the volume, timing, and spatial distribution of maximum SWE, mean SWE
 347 evolution tracked the nature run simulation significantly better than the open loop simulation in the spring snowmelt period.
 348 In fact, relative to the nature run, MAM SWE from the open loop simulations was biased high by approximately 63%, on

349 average, in the Upper Colorado (Table 2). The simulation with data assimilation using the forest strategy improved this bias
 350 to less than 1%, on average, over the same period. In this study, simulations using Noah-MP (open loop and data
 351 assimilation simulations) melted snow more rapidly in the later-half of the spring snowmelt season than the nature run
 352 simulation which evolved SWE using SnowModel (Section 2.1). Therefore, although maximum SWE volume, maximum
 353 SWE timing, and MAM SWE were improved by data assimilation, the timing of snow disappearance for the simulation with
 354 data assimilation using the forest strategy was approximately 18 days earlier than the nature run in the Upper Colorado.



355

356 **Figure 7.** Time series comparison of mean SWE (top) and total runoff (bottom) between the open loop, nature run, and
 357 simulations assimilating the synthetic observations, both with and without the forest strategy in the Upper Colorado. Dashed
 358 bars in the top plot represent the monthly percentage of the Upper Colorado grid cells with no snowmelt. Solid bars also
 359 exclude grid cells with forest coverage.

360 Much like the Upper Colorado, SWE simulated by the open loop simulation in the Pacific Northwest (Fig. S7) was biased
 361 high for the entirety of the snow season. Both domains also had greater than 80% synthetic snow observation coverage in
 362 March (including grid cells that filled snow estimates using the forest strategy), and as a result, the simulation with data

363 assimilation using the forest strategy closely matched SWE from the nature run. However, both of these domains had a
364 significant portion of the seasonal snowpack in forested landcover (Fig. 7 and Fig. S7, difference between the hatched and
365 solid bars). These grid cells had winter SWE estimates from the open loop simulation that were predominately high-biased
366 (Fig. 3 and Fig. 5). Therefore, although data assimilation improved winter SWE in non-forested landcover types (Fig. 6), the
367 simulation without the forest strategy caused little-to-no improvement in the simulated domain mean maximum SWE (Table
368 2). This highlights the value of the forest strategy used here (Fig. 2), which drew information from synthetic observations in
369 relatively few nearby pixels to infer the mean snow volume in forested grid cells. Given the four hydrologic regions
370 investigated in this study, a far smaller volume of snow existed in forested landcover for the California (Fig. S8) and Great
371 Basin regions (Fig. S6), resulting in DJF domain-mean SWE evolution that was more similar between the simulations with
372 and without the forest strategy. We expect results in these domains to be more indicative of the value of winter SAR
373 observations in less-vegetated snowy landscapes, such as Tundra and Prairie snow regimes (Sturm and Liston, 2021).

374 Finally, the improvements to the spatial and temporal estimates of SWE discussed above had trickle-down improvements
375 on simulated runoff. For example, in the Upper Colorado (Fig. 7), total annual runoff from the open loop simulation was
376 biased high by approximately 35%, relative to the nature run. This error was driven most by high-biased winter snow
377 accumulation, which nearly doubled the melt season (March – July) runoff estimated by the nature run simulation. Here, by
378 assimilating the synthetic SWE observations, and estimating forest snowpack from the relationship between modeled and
379 observed SWE from the nearest canopy-free pixels, total annual streamflow in this domain was improved to within 1%. Not
380 only was domain total runoff improved, but the seasonal evolution of high and low-flows vital for water management and
381 planning was also improved. This improved the Nash-Sutcliffe Efficiency (NSE) from -2.59 to 0.22 between the open loop
382 simulation and simulation with data assimilation employing the forest strategy (Table 2). These results were similar for the
383 Pacific Northwest, which had an NSE that improved from -0.17 to 0.39 . However, due to the smaller changes to SWE and
384 more-rapid snowmelt simulated by Noah-MP, changes to runoff from data assimilation in California and the Great Basin
385 were small (Table 2), with improvements that were largely outweighed by the difference in snowmelt timing and rates
386 between Noah-MP and SnowModel.

387 **4. Discussion**

388 The differences between the open loop simulation and nature run in this study were representative of snow modeling errors
389 common for continental and global-scale models used for seasonal to long-term future snow predictions (e.g., Franz et al.,
390 2010; Garousi-Nejad and Tarboton, 2022; Kim et al, 2021; Liu et al, 2022). The greatest source of these snow modeling errors
391 is commonly errors in meteorological forcing data, and in particular, biases in precipitation (Garousi-Nejad and Tarboton,
392 2022; Henn et al., 2018; Pflug et al., 2021; Raleigh and Lundquist, 2012; Wayand et al., 2013). These biases are especially
393 prevalent in the portions of the earth's surface with the greatest volumes of snow, such as the tundra and montane regions (Kim
394 et al., 2021), where ground observations and observation station maintenance are hindered by harsh winter conditions and

395 inaccessibility. This suggests that the greatest need for improving global estimates of snow is improved estimates of snow
396 accumulation in remote, under sampled landscapes. Here, we expect that the SAR observations evaluated in this study could
397 address these needs, thus providing a path forward for pairing common snow models with observations as a basis for
398 determining global snow mass. For example, assimilating SAR observations at 10 – 14 day intervals with the observational
399 error characteristics reported in Sect. 2.2, improved midlatitude winter SWE volume by approximately 22%, on average (Table
400 2). In unforested landscapes, which account for a majority of the Earth’s snow water storage (Kim et al., 2021), assimilation
401 improved the mean SWE bias at maximum SWE timing to within 1%, on average, and reduced the standard deviation of errors
402 by approximately 45 mm (~85%) (Fig. 6).

403 Despite the benefits discussed above, SAR observations have known limitations in forested landscapes where the canopy
404 overstory obstructs retrievals from the underlying snowpack (Huang et al., 2019; Ruiz et al., 2022; Tsang et al., 2022).
405 Therefore, this study was designed to investigate a forest strategy that uses the relationship between modeled SWE estimates
406 and synthetic SWE observations from neighboring grid cells as the basis for inferring snow distribution in regions with forested
407 landcover (Fig. 2). To focus on the benefits of this approach, we chose a domain (Fig. 1) that included both significant forest
408 spatial coverage (22%) with disproportionate amounts of winter snow (34%) within the forested pixels (Fig. 6). Relative to the
409 open loop simulation, the simulation with data assimilation and the forest strategy dramatically improved the spatial
410 distribution of SWE (e.g., Fig. 3 and Fig. 4) and the resulting SWE biases at domain maximum snowpack timing (Fig. 5). In
411 fact, in forested grid cells, SWE on 13 March was only biased by 14 mm (mean absolute error of 27 mm), on average, for the
412 simulation with data assimilation and the forest strategy, relative to the nature run. This was opposed to the open loop
413 simulation, which was biased by 87 mm (mean absolute error of 111 mm) over the same regions and date. Despite the fact that
414 the two simulations with data assimilation agreed in all grid cells except forested grid cells, the simulation employing the forest
415 strategy had a mean absolute error (17 mm) across the full modeling region that was approximately 51% smaller than the
416 simulation without the forest strategy. Here, we recognize that this study used a single date (13 March) to represent snow water
417 resources at maximum SWE timing. However, the date of maximum SWE volume from the nature run varied by less than a
418 week across the four hydrologic regions (11 - 16 March; Fig. 7, Fig. S6 - S8). Therefore, this was a relevant date for model
419 comparisons, especially given that water resource and allocation decisions in the Western US are often based on the volume
420 of snow at maximum snow timing.

421 This research shows how a modeling framework and relatively few observations can be used to gap-fill estimates of snow
422 in regions where remote sensing observations from a future platform may be most challenged. Despite the fact that snowpack
423 with properties able to be retrieved by SAR instrumentation (i.e., canopy-free landcover and no snowmelt) sometimes only
424 accounted for only small portions of a modeling domain (e.g., Fig. 7), SWE from the model and SAR observations in nearby
425 canopy-free grid cells were predictive of the snow in forested grid cells. We hypothesize that this could have partly been driven
426 by the 250 m resolution of synthetic observations and simulations. At this length scale, snow distribution is typically driven

427 by processes like mesoscale weather patterns and their interaction (e.g., orographic lapse rates, wind loading/sheltering, terrain-
428 shading, etc.) with static topographical features like elevation, slope, and aspect (e.g., Clark et al., 2011; Lehning et al., 2011;
429 McGrath et al., 2018; Minder et al., 2008; Trujillo et al., 2007). However, we acknowledge that snow in forested and open grid
430 cells is subject to different snow processes. In fact, the nature run simulation used here attempts to simulate snow-canopy
431 interactions, such as snow interception and solar shading from the canopy overstory (Liston and Elder, 2006). Here, since we
432 focus predominantly on model improvements from data assimilation in the SWE accumulation season, we hypothesize that
433 the primary difference between SWE accumulation in forested pixels, and the nearest canopy-free grid cells could be driven
434 by canopy interception, or the lack thereof. In other words, inferring forested snowpack using the nearest canopy-free grid
435 cells could bias snow in forested regions where snow processes differ slightly. While the forest strategy improved SWE
436 simulated in forested grid cells at the date of maximum SWE volume, SWE was still biased high relative to the nature run
437 (Fig. 6). We hypothesize that a correction factor, based on variables like forest canopy type, vegetation density, wind speed,
438 and temperature during snowfall, all of which influence snow interception (Lundquist et al., 2021), could be used to facilitate
439 the difference in snow accumulation expected between a forest pixel and SWE observations from nearby canopy-free grid
440 cells. This approach will be a topic of future research. However, since errors with precipitation are often the overwhelming
441 source of model errors, we hypothesize that the forest strategy (Fig. 2), which corrected modeled SWE in forested areas using
442 the ratio between modeled and observed SWE in nearby open areas, was well-suited to correct precipitation biases.

443 The results presented here are subject to a number of assumptions. These assumptions were intended to apply regionally-
444 consistent and conservative rules about how 1) synthetic SAR observations were generated, and 2) the grid cells and time
445 periods that SAR observations occurred in. For example, we used a 20% and zero-mean random distribution of errors to
446 generate observations from the nature run. We expect the error from a future satellite mission to be less than 20% over the
447 majority of snow covered regions (Sect. 2.2). However, observational biases may be more common in certain locations and
448 periods based on snow depth, particularly in very shallow or very deep snowpacks, terrain characteristics and vegetation
449 characteristics. Additionally, the landcover classification used in this study (Fig. 1) was based on the dominant landcover type
450 within each model grid cell, as defined from the North American Land Change Monitoring System (Latifovic et al., 2017). For
451 forested grid cells, this included needleleaf, broadleaf, and mixed forest types. To be conservative, this study completely
452 masked synthetic observations in 250 m grid cells classified as forest, thereby assuming 1) no observation capabilities in
453 predominantly forested areas, and 2) full observation capabilities in grid cells where forests were not the dominant landcover
454 type. In reality, SAR may be able to achieve accurate snow retrievals in some forested-dominated regions based on the forest
455 type, forest distribution, and canopy density (Tsang et al., 2022). Conversely, some regions with sparser or no forest cover
456 may still have observation limitations based on the domain and snow characteristics mentioned above. The large domain used
457 in this study also made tests over multiple years computationally challenging. Here, the intent of this study was to investigate
458 a strategy for deriving SWE corrections in difficult to observe forest landscapes, and we hypothesize that precipitation biases
459 and the resulting modeled SWE accumulation could be improved to a similar degree in years with both larger and smaller

460 snow volumes. Finally, while strategies for identifying and correcting systematic SAR observation errors are a topic of
461 continued research (e.g., Durand et al., 2023; Singh et al., 2023), OSSEs are an inherently flexible framework for evaluating
462 sensor utility, so future research could use the simulations performed here to test a wider array of sensor configurations and
463 non-normal retrieval errors. Future work could build upon these results to investigate multiple years, perhaps considering
464 warmer and/or drier snow years, when the role of snowpack for water supply and midwinter snowmelt and rain-on-snow
465 frequency may be more likely to increase snowpack liquid water content, or years with late-season spring snow accumulation.
466 Future research should also investigate other gap-filling approaches, like methods to infer SWE in grid cells where snowmelt
467 is occurring and liquid water may prevent SAR retrievals, and gap-filling approaches using different window sizes and/or
468 searching windows that more heavily weight unforested grid cells with similar characteristics (elevation, aspect, etc.).

469 This study tested a simple model setup using a popular land surface model (Noah-MP) and Kalman-based data assimilation
470 procedure. This data assimilation procedure updated modeled snow states, like snow depth and SWE, based only on synthetic
471 SWE observations at 10 – 14 day temporal frequencies where/when snowmelt was not occurring. Despite the limitations and
472 assumptions discussed above, we expect that the results presented here could represent the lower-bound of performance that
473 could be achieved from a real-time modeling framework that could accompany a space-borne SAR remote sensing platform.
474 For example, many studies have demonstrated repeatable patterns of snow accumulation in years with similar winter
475 meteorological characteristics (e.g., Deems et al., 2008; Pflug et al., 2022; Schirmer et al., 2011; Sturm and Wagner, 2010;
476 Woodruff and Qualls, 2019). This suggests that retrospective information about snow distribution patterns in previous years,
477 could be used as the basis for extrapolating and updating snow model states in grid cells not covered by SAR observations on
478 a given date. From the modeling perspective, only 5 ensemble members were used in the Ensemble-Kalman data assimilation
479 (Sec 2.3), when a larger ensemble of simulations may have improved uncertainty characterization of simulated snow and
480 hydrological states even more. This study also assumed that synthetic SAR observations were unable to observe snow in all
481 forested landscapes, when retrievals of snow in forested stands could be achievable for some forested regions with smaller tree
482 cover fractions and biomass (Montomoli et al., 2015; Tsang et al., 2022). Finally, the SAR configuration tested here had 10 –
483 14 day repeat times, but future satellite configurations with more-frequent observational repeats are possible and have been
484 recommended by the 2018 Decadal Survey (NASEM 2018). Despite all of these conservative assumptions, the difference
485 between the open loop simulation (representative of current modeling accuracies), and the simulation with synthetic
486 observation data assimilation using the forest strategy, demonstrated large-magnitude and widespread improvements to real-
487 time estimates of winter SWE and the associated improvement to spring SWE and runoff. Therefore, we expect the findings
488 of this study, particularly the strategy to extend the observational utility to forested areas, to significantly aid in the full
489 exploitation of the information from a future SAR-based snow satellite mission.

490 5. Conclusion

491 Global estimates of snow volume and distribution have uncertainties stemming from limited snow observations and
492 biases in meteorological forcing data. These uncertainties stress the need for a global snow-focused satellite remote
493 sensing platform. Here, we investigate the degree to which synthetic observations of SWE representative of a Synthetic
494 Aperture Radar (SAR) remote sensing platform, could correct common snow modeling errors and provide
495 spatiotemporally continuous SWE estimates. We investigate this using an Observing System Simulation Experiment,
496 specifically investigating how much snow simulated using a widely used land surface model and meteorological forcing
497 dataset, could be improved by assimilating synthetic SAR observations of SWE.

498 The difference between the open loop simulation and the nature run was representative of common modeling errors.
499 Snow simulated by the open loop simulation had larger winter snow extents, and total snow volume that was biased high
500 by approximately 35%. The open loop simulation also simulated snow that was more spatially homogeneous,
501 underestimating the variability across variations in topography and underestimating lower-elevation snowmelt from the
502 nature run. Assimilating the synthetic SWE observations improved SWE simulated in the shrub, grass, crop, bare-ground,
503 and wetland land cover types. In fact, SWE biases on the date of domain maximum SWE volume (13 March 2019) in
504 these landcover types improved from 14% for the open loop simulation to within 1% after data assimilation. However,
505 despite only covering 22% of the study area, forested grid cells contained just over 34% of the domain SWE on 13
506 March. The open loop simulation and the simulation with data assimilation without the forest strategy had SWE that was
507 high biased by 150% (87 mm), on average, in these forested grid cells. The relationship between modeled SWE and
508 synthetic SWE observations in forested grid cells exhibited similarities with the nearest canopy-free grid cells. Therefore,
509 SWE in forested regions was able to be inferred using the simple modeling framework and synthetic SAR observations
510 from nearby canopy-free grid cells. In fact, the simulation with data assimilation using this forest gap-filling strategy
511 substantially improved SWE biases to 4% (~22% improvement) at maximum SWE timing, with a SWE mean absolute
512 error of 17 mm (24 mm improvement) and spatial correlation of 0.91 (0.17 improvement) across the Western US

513 Improvements in winter SWE accumulation also improved estimates of melt-season SWE evolution and total runoff
514 in four major Western US hydrologic regions, even in periods when winter snowmelt greatly reduced the number of grid
515 cells that could be observed by the synthetic SWE observations. In fact, in the Upper Colorado River, melt season SWE
516 biases improved from 63% to less than 1% after assimilation, and the runoff Nash Sutcliffe Efficiency improved from -
517 2.59 to 0.22. These results demonstrate the value of SAR observations and simple spatial-filling strategies in grid cells
518 where SAR retrievals could be obstructed by the canopy. Here, we expect our results to represent a lower-boundary of
519 model performance which could be improved further by more robust assimilation approaches, more-frequent SAR
520 observations, further developments to SAR retrieval algorithms in forested landscapes, and adaptations to the forest gap-

521 filling strategy developed here. However, our results also show that widespread improvements to global SWE could be
522 available in near real-time provided data assimilation approaches and a SAR remote sensing platform.

523 *Code availability:* The Land Information System (LIS; lis.gsfc.nasa.gov) framework used to perform the nature run, open
524 loop, and data assimilation simulations from this study can be accessed from a GitHub public repository
525 (<https://github.com/NASA-LIS/LISF>). Model documentation and LIS tutorials can also be accessed from this repository. Users
526 are encouraged to reference Kumar et al. (2006) for more information on LIS. The Trade-space Analysis Tool for designing
527 Constellations (TAT-C) tool is currently available on-request for federal employees and contractors
528 (<https://software.nasa.gov/software/GSC-18399-1>).

529 *Data availability:* The model outputs and data necessary to reproduce the figures and statistics reported in this study can
530 be found at <https://www.hydroshare.org/resource/e0ad80f818bf4062a335e9e0d7362834/>. This repository includes
531 domain static variables, such as land cover, elevation, and spatial coordinates, in addition to model outputs of winter-average
532 SWE, SWE at the date of maximum SWE volume (13 March 2019), and SWE and runoff aggregated across each region.
533 MERRA-2 forcing data can be accessed from the Goddard Earth Sciences Data and Information Services Center (GES DISC,
534 <https://disc.gsfc.nasa.gov/>), and ERA5 data can be accessed from the European Centre for Medium-Range Weather Forecasts
535 climate data store (<https://www.ecmwf.int/en/forecasts/dataset/ecmwf-reanalysis-v5>).

536 *Author contributions:* CV and SK coordinated the manuscript question and research methodology. SK adapted LIS model
537 source code to implement the forest gap-filling strategy in Sect. 2.4. MW set up the model domains and model configurations,
538 and performed the open loop simulation. EC assisted with generating the synthetic SWE observations. With assistance from
539 KA, JP performed code developments for the simulations using both the Noah-MP and coupled SnowModel models. KA
540 implemented the SnowModel code and parameters into LIS and LDT. JP also performed the nature run and both data
541 assimilation simulations. The manuscript was written provided text, figures, and feedback from all coauthors.

542 *Competing interests:* The authors declare that they have no conflict of interest.

543 *Acknowledgements:* This work was supported by the funding from the NASA Terrestrial Hydrology program. Computing was
544 supported by the NASA Center for Climate Simulation (NCCS).

545 **References**

- 546 Arsenault, K.R., Wrzesien, M., Gutmann, E.D., Vuyovich, C., Liston, G.E., Mower, R., Reinking, A., Newman, A.J., Kumar,
547 S.V., Wang, S., Navari, M., Forman, B.A., Jessica, L.: Implementing SnowModel into the Land Information System
548 Framework to Support High Resolution Modeling of Snow Heterogeneity. Presented at the AGU Fall Meeting 2021,
549 AGU, 2021.
- 550 Barnett, T.P., Adam, J.C., Lettenmaier, D.P.: Potential impacts of a warming climate on water availability in snow-dominated
551 regions. *Nature* 438, 303. <https://doi.org/10.1038/nature04141>, 2005.

- 552 Barry, R.G.: The Role of Snow and Ice in the Global Climate System: A Review. *Polar Geography* 26, 235–246.
553 <https://doi.org/10.1080/789610195>, 2002.
- 554 Best, M.J., Pryor, M., Clark, D.B., Rooney, G.G., Essery, R.L.H., Ménard, C.B., Edwards, J.M., Hendry, M.A., Porson, A.,
555 Gedney, N., Mercado, L.M., Sitch, S., Blyth, E., Boucher, O., Cox, P.M., Grimmond, C.S.B., Harding, R.J.: The Joint
556 UK Land Environment Simulator (JULES), model description – Part 1: Energy and water fluxes. *Geoscientific Model*
557 *Development* 4, 677–699. <https://doi.org/10.5194/gmd-4-677-2011>, 2011.
- 558 Beven, K.J., Kirby, M.J., Freer, J.E., Lamb, R.: A history of TOPMODEL. *Hydrology and Earth System Sciences* 25, 527–549.
559 <https://doi.org/10.5194/hess-25-527-2021>, 2021.
- 560 Cho, E., Vuyovich, C. M., Kumar, S. V., Wrzesien, M. L., & Kim, R. S. (2023). Evaluating the utility of active microwave
561 observations as a snow mission concept using observing system simulation experiments. *The Cryosphere*, 17(9),
562 3915–3931.
- 563 Clark, M.P., Hendrikx, J., Slater, A.G., Kavetski, D., Anderson, B., Cullen, N.J., Kerr, T., Hreinsson, E.Ö., Woods, R.A.:
564 Representing spatial variability of snow water equivalent in hydrologic and land-surface models: A review. *Water*
565 *Resources Research* 47. <https://doi.org/10.1029/2011WR010745>, 2011.
- 566 Cosgrove, B.A., Lohmann, D., Mitchell, K.E., Houser, P.R., Wood, E.F., Schaake, J.C., Robock, A., Marshall, C., Sheffield,
567 J., Duan, Q., Luo, L.: Real-time and retrospective forcing in the North American Land Data Assimilation System
568 (NLDAS) project. *Journal of Geophysical Research: Atmospheres*, 108.D22, 2003.
- 569 De Lannoy, G.J.M., Reichle, R.H., Arsenault, K.R., Houser, P.R., Kumar, S., Verhoest, N.E.C., Pauwels, V.R.N.: Multiscale
570 assimilation of Advanced Microwave Scanning Radiometer–EOS snow water equivalent and Moderate Resolution
571 Imaging Spectroradiometer snow cover fraction observations in northern Colorado. *Water Resources Research* 48.
572 <https://doi.org/10.1029/2011WR010588>, 2012.
- 573 Deems, J.S., Fassnacht, S.R., Elder, K.J.: Interannual Consistency in Fractal Snow Depth Patterns at Two Colorado Mountain
574 Sites. *J. Hydrometeorol* 9, 977–988. <https://doi.org/10.1175/2008JHM901.1>, 2008.
- 575 Derksen, C., Lemmetyinen, J., Toose, P., Silis, A., Pulliainen, J., Sturm, M.: Physical properties of arctic versus subarctic
576 snow: Implications for high latitude passive microwave snow water equivalent retrievals. *Journal of Geophysical*
577 *Research: Atmospheres* 119, 7254 – 7270. <https://doi.org/10.1002/2013JD021264>, 2014.
- 578 Durand, M., Johnson, J.T., Dechow, J., Tsang, L., Borah, F., Kim, E.J.: Retrieval of SWE from dual-frequency radar
579 measurements: Using time series to overcome the need for accurate a priori information. *EGU sphere* 1 – 23.
580 <https://doi.org/10.5194/egusphere-2023-1653>, 2023.
- 581 Ek, M.B., Mitchell, K.E., Lin, Y., Rogers, E., Grunmann, P., Koren, V., Gayno, G., Tarpley, J.D.: Implementation of Noah
582 land surface model advances in the National Centers for Environmental Prediction operational mesoscale Eta model.
583 *Journal of Geophysical Research: Atmospheres* 108. <https://doi.org/10.1029/2002JD003296>, 2003.
- 584 Errico, R.M., Yang, R., Masutani, M., Woollen, J.S.: The estimation of analysis error characteristics using an observation
585 systems simulation experiment. *Meteorologische Zeitschrift* 16, 695–708, 2007.
- 586 Fang, Y., Liu, Y., Margulis, S.A.: A western United States snow reanalysis dataset over the Landsat era from water eyars 1985
587 to 2021. *Sci Data* 9, 677. <https://doi.org/10.1038/s41597-022-01768-7>, 2022.
- 588 Foster, J.L., Sun, C., Walker, J.P., Kelly, R., Chang, A., Dong, J., Powell, H.: Quantifying the uncertainty in passive microwave
589 snow water equivalent observations. *Remote Sensing of the Environment* 94, 187 – 203.
590 <https://doi.org/10.1016/j.rse.2004.09.012>, 2005.
- 591 Franz, K.J., Butcher, P., Ajami, N.K.: Addressing snow model uncertainty for hydrologic prediction. *Advances in Water*
592 *Resources* 33, 820–832. <https://doi.org/10.1016/j.advwatres.2010.05.004>, 2010.
- 593 Garnaud, C., Bélair, S., Carrera, M.L., Derksen, C., Bilodeau, B., Abrahamowicz, M., Gauthier, N., Vionnet, V.: Quantifying
594 Snow Mass Mission Concept Trade-Offs Using an Observing System Simulation Experiment. *Journal of*
595 *Hydrometeorology* 20, 155–173. <https://doi.org/10.1175/JHM-D-17-0241.1>, 2019.
- 596 Garousi-Nejad, I., Tarboton, D.G.: A comparison of National Water Model retrospective analysis snow outputs at snow
597 telemetry sites across the Western United States. *Hydrological Processes* 36, e14469.
598 <https://doi.org/10.1002/hyp.14469>, 2022.
- 599 Gelaro, R., McCarty, W., Suárez, M.J., Todling, R., Molod, A., Takacs, L., Randles, C.A., Darmenov, A., Bosilovich, M.G.,
600 Reichle, R., Wargan, K., Coy, L., Cullather, R., Draper, C., Akella, S., Buchard, V., Conaty, A., Silva, A.M. da, Gu,
601 W., Kim, G.-K., Koster, R., Lucchesi, R., Merkova, D., Nielsen, J.E., Partyka, G., Pawson, S., Putman, W., Rienecker,

602 M., Schubert, S.D., Sienkiewicz, M., Zhao, B.: The Modern-Era Retrospective Analysis for Research and
603 Applications, Version 2 (MERRA-2). *Journal of Climate* 30, 5419–5454. <https://doi.org/10.1175/JCLI-D-16-0758.1>,
604 2017.

605 Henn, B., Newman, A.J., Livneh, B., Daly, C., Lundquist, J.D.: An assessment of differences in gridded precipitation datasets
606 in complex terrain. *Journal of Hydrology* 556, 1205–1219. <https://doi.org/10.1016/j.jhydrol.2017.03.008>, 2018.

607 Hersbach, H., Bell, B., Berrisford, P., Hirahara, S., Horányi, A., Muñoz-Sabater, J., Nicolas, J., Peubey, C., Radu, R., Schepers,
608 D., Simmons, A., Soci, C., Abdalla, S., Abellan, X., Balsamo, G., Bechtold, P., Biavati, G., Bidlot, J., Bonavita, M.,
609 De Chiara, G., Dahlgren, P., Dee, D., Diamantakis, M., Dragani, R., Flemming, J., Forbes, R., Fuentes, M., Geer, A.,
610 Haimberger, L., Healy, S., Hogan, R.J., Hólm, E., Janisková, M., Keeley, S., Laloyaux, P., Lopez, P., Lupu, C.,
611 Radnoti, G., de Rosnay, P., Rozum, I., Vamborg, F., Villaume, S., Thépaut, J.-N.: The ERA5 global reanalysis.
612 *Quarterly Journal of the Royal Meteorological Society* 146, 1999–2049. <https://doi.org/10.1002/qj.3803>, 2020.

613 Hiemstra, C.A., Liston, G.E., Reiners, W.A.: Snow Redistribution by Wind and Interactions with Vegetation at Upper Treeline
614 in the Medicine Bow Mountains, Wyoming, U.S.A. *Arctic, Antarctic, and Alpine Research* 34, 262–273.
615 <https://doi.org/10.1080/15230430.2002.12003493>, 2002.

616 Huang, H., Tsang, L., Colliander, A., Yueh, S.H.: Propagation of Waves in Randomly Distributed Cylinders Using Three-
617 Dimensional Vector Cylindrical Wave Expansions in Foldy–Lax Equations. *IEEE Journal on Multiscale and*
618 *Multiphysics Computational Techniques* 4, 214–226. <https://doi.org/10.1109/JMMCT.2019.2948022>, 2019.

619 Kim, R.S., Kumar, S., Vuyovich, C., Houser, P., Lundquist, J., Mudryk, L., Durand, M., Barros, A., Kim, E.J., Forman, B.A.,
620 Gutmann, E.D., Wrzesien, M.L., Garnaud, C., Sandells, M., Marshall, H.-P., Cristea, N., Pflug, J.M., Johnston, J.,
621 Cao, Y., Mocko, D., Wang, S.: Snow Ensemble Uncertainty Project (SEUP): quantification of snow water equivalent
622 uncertainty across North America via ensemble land surface modeling. *The Cryosphere* 15, 771–791.
623 <https://doi.org/10.5194/tc-15-771-2021>, 2021.

624 Koster, R.D., Mahanama, S.P.P., Livneh, B., Lettenmaier, D.P., Reichle, R.H.: Skill in streamflow forecasts derived from
625 large-scale estimates of soil moisture and snow. *Nature Geosci* 3, 613–616. <https://doi.org/10.1038/ngeo944>, 2010.

626 Koster, R.D., Suarez, M.J., Ducharme, A., Stieglitz, M., Kumar, P.: A catchment-based approach to modeling land surface
627 processes in a general circulation model: 1. Model structure. *Journal of Geophysical Research: Atmospheres* 105,
628 24809–24822. <https://doi.org/10.1029/2000JD900327>, 2000.

629 Kumar, S.V., Kolassa, J., Reichle, R., Crow, W., de Lannoy, G., de Rosnay, P., MacBean, N., Giroto, M., Fox, A., Quaife,
630 T., Draper, C., Forman, B., Balsamo, G., Steele-Dunne, S., Albergel, C., Bonan, B., Calvet, J.-C., Dong, J., Liddy,
631 H., Ruston, B.: An Agenda for Land Data Assimilation Priorities: Realizing the Promise of Terrestrial Water, Energy,
632 and Vegetation Observations From Space. *Journal of Advances in Modeling Earth Systems* 14, e2022MS003259.
633 <https://doi.org/10.1029/2022MS003259>, 2022.

634 Kumar, S.V., Peters-Lidard, C.D., Tian, Y., Houser, P.R., Geiger, J., Olden, S., Lighty, L., Eastman, J.L., Doty, B., Dirmeyer,
635 P., Adams, J., Mitchell, K., Wood, E.F., Sheffield, J.: Land information system: An interoperable framework for high
636 resolution land surface modeling. *Environmental Modelling & Software* 21, 1402–1415.
637 <https://doi.org/10.1016/j.envsoft.2005.07.004>, 2006.

638 Kumar, S.V., Peters-Lidard, C.D., Mocko, D., Tian, Y.: Multiscale Evaluation of the Improvements in Surface Snow
639 Simulation through Terrain Adjustments to Radiation. *Journal of Hydrometeorology* 14, 220–232.
640 <https://doi.org/10.1175/JHM-D-12-046.1>, 2013.

641 Kwon, Y., Yoon, Y., Forman, B.A., Kumar, S.V., Wang, L.: Quantifying the observational requirements of a space-borne
642 LiDAR snow mission. *Journal of Hydrology* 601, 126709. <https://doi.org/10.1016/j.jhydrol.2021.126709>, 2021.

643 Lahmers, T.M., Kumar, S.V., Rosen, D., Dugger, A., Gochis, D.J., Santanello, J.A., Gangodagamage, C., Dunlap, R.:
644 Assimilation of NASA’s Airborne Snow Observatory Snow Measurements for Improved Hydrological Modeling: A
645 Case Study Enabled by the Coupled LIS/WRF-Hydro System. *Water Resources Research* 58, e2021WR029867.
646 <https://doi.org/10.1029/2021WR029867>, 2022.

647 Latifovic, R., Pouliot, D., Olthof, I.: Circa 2010 Land Cover of Canada: Local optimization methodology and product
648 development. *Remote Sensing* 9, 11. <https://doi.org/10.3390/rs9111098>, 2017.

649 Le Moigne, J., Dabney, P., de Weck, O., Foreman, V., Grogan, P., Holland, M., Hughes, S., Nag, S.: Tradespace analysis tool
650 for designing constellations (TAT-C), in: 2017 IEEE International Geoscience and Remote Sensing Symposium
651 (IGARSS). IEEE, pp. 1181–1184, 2017.

652 Lehning, M., Grünewald, T., Schirmer, M.: Mountain snow distribution governed by an altitudinal gradient and terrain
653 roughness. *Geophysical Research Letters* 38. <https://doi.org/10.1029/2011GL048927>, 2011.

654 Li, D., Wrzesien, M.L., Durand, M., Adam, J., Lettenmaier, D.P.: How much runoff originates as snow in the western United
655 States, and how will that change in the future? *Geophysical Research Letters* 44, 6163–6172.
656 <https://doi.org/10.1002/2017GL073551>, 2017.

657 Liang, X., Lettenmaier, D.P., Wood, E.F., Burges, S.J.: A simple hydrologically based model of land surface water and energy
658 fluxes for general circulation models. *Journal of Geophysical Research: Atmospheres* 99, 14415–14428.
659 <https://doi.org/10.1029/94JD00483>, 1994.

660 Lievens, H., Demuzere, M., Marshall, H.P., Reichle, R.H., Brucker, L., de Rosnay, P., Dumont, M., Giroto, M., Immerzeel,
661 W.W., Jonas, T., Kim, E.J., Koch, I., Marty, C., Saloranta, T., Schober, J., De Lannoy, G.J.M.: Snow depth variability
662 in the Northern Hemisphere mountains observed from space. *Nature Communications*, 2019.

663 Liston, G.E., Elder, K.: A Distributed Snow-Evolution Modeling System (SnowModel). *Journal of Hydrometeorology* 7,
664 1259–1276. <https://doi.org/10.1175/JHM548.1>, 2006.

665 Liston, G.E., Perham, C.J., Shideler, R.T., Chevront, A.N.: Modeling snowdrift habitat for polar bear dens. *Ecological*
666 *Modelling* 320, 114–134. <https://doi.org/10.1016/j.ecolmodel.2015.09.010>, 2016.

667 Liu, Y., Fang, Y., Li, D., Margulis, S.A.: How well do global snow products characterize snow storage in high mountain Asia?
668 *Geophysical Research Letters* 49, e2022GL100082. <https://doi.org/10.1029/2022GL100082>, 2022.

669 Livneh, B., Badger, A.M.: Drought less predictable under declining future snowpack. *Nat. Clim. Chang.* 10, 452–458.
670 <https://doi.org/10.1038/s41558-020-0754-8>, 2020.

671 Lundquist, J.D., Dickerson-Lange, S., Gutmann, E., Jonas, T., Lumbrazo, C., Reynolds, D.: Snow interceptions modelling:
672 Isolated observations have led to many land surface models lacking appropriate temperature sensitivities.
673 *Hydrological Processes* 35, 7. <https://doi.org/10.1002/hyp.14274>, 2021.

674 Mahoney, P.J., Liston, G.E., LaPoint, S., Gurarie, E., Mangipane, B., Wells, A.G., Brinkman, T.J., Eitel, J.U.H., Hebblewhite,
675 M., Nolin, A.W., Boelman, N., Prugh, L.R.: Navigating snowscapes: scale-dependent responses of mountain sheep
676 to snowpack properties. *Ecological Applications* 28, 1715–1729. <https://doi.org/10.1002/eap.1773>, 2018.

677 McGrath, D., Sass, L., O’Neel, S., McNeil, C., Candela, S.G., Baker, E.H., Marshall, H.P.: Interannual snow accumulation
678 variability on glaciers derived from repeat, spatially extensive ground-penetrating radar surveys. *The Cryosphere* 12,
679 3617–3633. <https://doi.org/10.5194/tc-12-3617-2018>, 2018.

680 Mernild, S.H., Liston, G.E., Hiemstra, C., Wilson, R.: The Andes Cordillera. Part III: glacier surface mass balance and
681 contribution to sea level rise (1979–2014). *International Journal of Climatology* 37, 3154–3174.
682 <https://doi.org/10.1002/joc.4907>, 2017.

683 Minder, J.R., Durran, D.R., Roe, G.H., Anders, A.M.: The climatology of small-scale orographic precipitation over the
684 Olympic Mountains: Patterns and processes. *Quarterly Journal of the Royal Meteorological Society* 134, 817–839.
685 <https://doi.org/10.1002/qj.258>, 2008.

686 Montomoli, F., Macelloni, G., Brogioni, M., Lemmetyinen, J., Cohen, J., Rott, H.: Observations and simulation of
687 multifrequency SAR data over a snow-covered boreal forest. *IEEE journal of selected topics in applied earth*
688 *observations and remote sensing* 9, 1216–1228, 2015.

689 NASM: National Academies of Sciences, Engineering, and Medicine: Thriving on our changing planet: A decadal strategy for
690 Earth observation from space. Washington, DC: The National Academies Press. doi: <https://doi.org/10.17226/24938>,
691 2018.

692 Niu, G., Yang, Z., Mitchell, K.E., Chen, F., Ek, M.B., Barlage, M., Kumar, A., Manning, K., Niyogi, D., Rosero, E., Tewari,
693 M., Xia, Y.: The community Noah land surface model with multiparameterization options (Noah-MP): 1. Model
694 description and evaluation with local-scale measurements. *Journal of Geophysical Research: Atmospheres* 116.
695 <https://doi.org/10.1029/2010JD015139>, 2011.

696 Niu, G.-Y., Yang, Z.-L.: Effects of vegetation canopy processes on snow surface energy and mass balances. *Journal of*
697 *Geophysical Research: Atmospheres* 109. <https://doi.org/10.1029/2004JD004884>, 2004.

698 Painter, T.H., Berisford, D.F., Boardman, J.W., Bormann, K.J., Deems, J.S., Gehrke, F., Hedrick, A., Joyce, M., Laidlaw, R.,
699 Marks, D., Mattmann, C., McGurk, B., Ramirez, P., Richardson, M., Skiles, S.M., Seidel, F.C., Winstral, A.: The
700 Airborne Snow Observatory: Fusion of scanning lidar, imaging spectrometer, and physically-based modeling for

701 mapping snow water equivalent and snow albedo. *Remote Sensing of Environment* 184, 139–152.
702 <https://doi.org/10.1016/j.rse.2016.06.018>, 2016.

703 Pflug, J.M., Hughes, M., Lundquist, J.D.: Downscaling snow deposition using historic snow depth patterns: Diagnosing
704 limitations from snowfall biases, winter snow losses, and interannual snow pattern repeatability. *Water Resources*
705 *Research* e2021WR029999. <https://doi.org/10.1029/2021WR029999>, 2021.

706 Pflug, J.M., Margulis, S.A., Lundquist, J.D.: Inferring watershed-scale mean snowfall magnitude and distribution using
707 multidecadal snow reanalysis patterns and snow pillow observations. *Hydrological Processes* 36, e14581, 2022.

708 Raleigh, M.S., Lundquist, J.D.: Comparing and combining SWE estimates from the SNOW-17 model using PRISM and SWE
709 reconstruction. *Water Resources Research* 48. <https://doi.org/10.1029/2011WR010542>, 2012.

710 Reichle, R.H., McLaughlin, D.B., Entekhabi, D.: Hydrologic Data Assimilation with the Ensemble Kalman Filter. *Monthly*
711 *Weather Review* 130, 103–114. [https://doi.org/10.1175/1520-0493\(2002\)130<0103:HDAWTE>2.0.CO;2](https://doi.org/10.1175/1520-0493(2002)130<0103:HDAWTE>2.0.CO;2), 2002.

712 Rott, H., Yueh, S. H., Cline, D. W., Duguay, C., Essery, R., Haas, C., Hélière, F., Kern, M., Macelloni, G., Malnes, E.,
713 Thompson, A.: Cold regions hydrology high-resolution observatory for snow and cold land processes. *Proceedings*
714 *of the IEEE*, 98(5), 752–765, 2010.

715 Rott, H., Duguay, C., Etchevers, P., Essery, R., Hajnsek, I., Macelloni, G., Malnes, E., and Pulliainen, J.: CoReH2O Report
716 for mission selection: An Earth Explorer to observe snow and ice, Tech. rep., European Space Agency,
717 [https://earth.esa.int/eogateway/documents/20142/37627/CoReH2O-Report-for-Mission-Selection-An-Earth-](https://earth.esa.int/eogateway/documents/20142/37627/CoReH2O-Report-for-Mission-Selection-An-Earth-Explorer-to-observe-snow-and-ice.pdf)
718 [Explorer-to-observe-snow-and-ice.pdf](https://earth.esa.int/eogateway/documents/20142/37627/CoReH2O-Report-for-Mission-Selection-An-Earth-Explorer-to-observe-snow-and-ice.pdf), 2012.

719 Ruiz, J.J., Lemmetyinen, J., Kontu, A., Tarvainen, R., Vehmas, R., Pulliainen, J., Praks, J.: Investigation of Environmental
720 Effects on Coherence Loss in SAR Interferometry for Snow Water Equivalent Retrieval. *IEEE Transactions on*
721 *Geoscience and Remote Sensing* 60, 1–15. <https://doi.org/10.1109/TGRS.2022.3223760>, 2022.

722 Schirmer, M., Wirz, V., Clifton, A., Lehning, M.: Persistence in intra-annual snow depth distribution: 1. Measurements and
723 topographic control: PERSISTENT SNOW DEPTH DEVELOPMENT, 1. *Water Resources Research* 47.
724 <https://doi.org/10.1029/2010WR009426>, 2011.

725 Singh, S., Durand, M., Kim, E., Barros, A.P.: Bayesian physical-statistical retrieval of snow water equivalent and snow depth
726 from X- and Ku-band synthetic-aperture-radar demonstration using airborne SnowSAR in SnowEx17. *EGU sphere* 1
727 – 35. <https://doi.org/10.5194/egusphere-2023-1987>, 2023.

728 Sturm, M., Wagner, A.M.: Using repeated patterns in snow distribution modeling: An Arctic example. *Water Resources*
729 *Research* 46, 2010.

730 Terzago, S., Bongiovanni, G., von Hardenberg, J.: Seasonal forecasting of snow resources at Alpine sites. *Hydrology and Earth*
731 *System Sciences* 27, 519–542. <https://doi.org/10.5194/hess-27-519-2023>, 2023.

732 Trujillo, E., Ramírez, J.A., Elder, K.J.: Topographic, meteorologic, and canopy controls on the scaling characteristics of the
733 spatial distribution of snow depth fields. *Water Resources Research* 43, 2007.

734 Tsang, L., Durand, M., Derksen, C., Barros, A.P., Kang, D.-H., Lievens, H., Marshall, H.-P., Zhu, J., Johnson, J., King, J.,
735 Lemmetyinen, J., Sandells, M., Rutter, N., Siqueira, P., Nolin, A., Osmanoglu, B., Vuyovich, C., Kim, E., Taylor, D.,
736 Merkouriadi, I., Brucker, L., Navari, M., Dumont, M., Kelly, R., Kim, R.S., Liao, T.-H., Borah, F., Xu, X.: Review
737 article: Global monitoring of snow water equivalent using high-frequency radar remote sensing. *The Cryosphere* 16,
738 3531–3573. <https://doi.org/10.5194/tc-16-3531-2022>, 2022.

739 Wayand, N.E., Hamlet, A.F., Hughes, M., Feld, S.I., Lundquist, J.D.: Intercomparison of Meteorological Forcing Data from
740 Empirical and Mesoscale Model Sources in the North Fork American River Basin in Northern Sierra Nevada,
741 California. *Journal of Hydrometeorology* 14, 677–699. <https://doi.org/10.1175/JHM-D-12-0102.1>, 2013.

742 Woodruff, C.D., Qualls, R.J.: Recurrent Snowmelt Pattern Synthesis using Principal Component Analysis of Multi-Year
743 Remotely Sensed Snow Cover. *Water Resources Research* 55, 6869–6885. <https://doi.org/10.1029/2018WR024546>,
744 2019.

745 Wrzesien, M., Kumar, S.V., Vuyovich, C., Kim, R.S., Cho, E., Pflug, J.M., Konapala, G., Arsenault, K.R.: Merging remote
746 sensing and models to improve performance and accessibility of snow information, AGU Fall Meeting, Conference
747 on Hydrology, 2022.

748 Wrzesien, M.L., Kumar, S., Vuyovich, C., Gutmann, E.D., Kim, R.S., Forman, B.A., Durand, M., Raleigh, M.S., Webb, R.,
749 Houser, P.: Development of a “Nature Run” for Observing System Simulation Experiments (OSSEs) for Snow
750 Mission Development. *Journal of Hydrometeorology* 23, 351–375. <https://doi.org/10.1175/JHM-D-21-0071.1>, 2022.

751 Ying, Y.: Assimilating Observations with Spatially Correlated Errors Using a Serial Ensemble Filter with a Multiscale
752 Approach. *Monthly Weather Review* 148, 3397–3412. <https://doi.org/10.1175/MWR-D-19-0387.1>, 2020.

753 Yu, L., Fennel, K., Wang, B., Laurent, A., Thompson, K.R., Shay, L.K.: Evaluation of nonidentical versus identical twin
754 approaches for observation impact assessments: an ensemble-Kalman-filter-based ocean assimilation application for
755 the Gulf of Mexico. *Ocean Science* 15, 1801–1814. <https://doi.org/10.5194/os-15-1801-2019>, 2019.

756 Yueh, S. H., Dinardo, S. J., Akgiray, A., West, R., Cline, D. W., Elder, K.: Airborne Ku-band polarimetric radar remote
757 sensing of terrestrial snow cover. *IEEE Transactions on Geoscience and Remote Sensing*, 47(10), 3347-3364. 2009.

758 Zhu, J., Tan, S., King, J., Derksen, C., Lemmetyinen, J., and Tsang, L.: Forward and inverse radar modeling of terrestrial snow
759 using SnowSAR Data, *IEEE Transactions on Geoscience and Remote Sensing*, 56(12), 7122-7132,
760 [doi:10.1109/TGRS.2018.2848642](https://doi.org/10.1109/TGRS.2018.2848642), 2018.

761 Zhu, J., Tan, S., Tsang, L., Kang, D.K., and Kim, E.: Snow water equivalent retrieval using active and passive microwave
762 observations. *Water Resources Research* 57, no. 7, 2021.